

Implications for the origin of early-type dwarf galaxies – the discovery of rotation in isolated, low-mass early-type galaxies

Joachim Janz,^{1★} Samantha J. Penny,² Alister W. Graham,¹ Duncan A. Forbes¹ and Roger L. Davies³

¹*Centre for Astrophysics and Supercomputing, Swinburne University, Hawthorn, VIC 3122, Australia*

²*Institute of Cosmology and Gravitation, University of Portsmouth, Dennis Sciama Building, Burnaby Road, Portsmouth PO1 3FX, UK*

³*Sub-department of Astrophysics, Department of Physics, University of Oxford, Denys Wilkinson Building, Keble Road, Oxford OX1 3RH, UK*

Accepted 2017 March 10. Received 2017 March 2; in original form 2016 October 7

ABSTRACT

We present the discovery of rotation in quenched, low-mass early-type galaxies that are isolated. This finding challenges the claim that (all) rotating dwarf early-type galaxies in clusters were once spiral galaxies that have since been harassed and transformed into early-type galaxies. Our search of the Sloan Digital Sky Survey data within the Local Volume ($z < 0.02$) has yielded a sample of 46 galaxies with a stellar mass $M_* \lesssim 5 \times 10^9 M_\odot$ (median $M_* \sim 9.29 \times 10^8 M_\odot$), a low H α equivalent width $EW_{H\alpha} < 2 \text{ \AA}$, and no massive neighbour ($M_* \gtrsim 3 \times 10^{10} M_\odot$) within a velocity interval of $\Delta V = 500 \text{ km s}^{-1}$ and a projected distance of $\sim 1 \text{ Mpc}$. Nine of these galaxies were subsequently observed with Keck Echelle Spectrograph and Imager and their radial kinematics are presented here. These extend out to the half-light radius R_e in the best cases, and beyond $R_e/2$ for all. They reveal a variety of behaviours similar to those of a comparison sample of early-type dwarf galaxies in the Virgo cluster observed by Toloba et al. Both samples have similar frequencies of slow and fast rotators, as well as kinematically decoupled cores. This, and especially the finding of rotating quenched low-mass galaxies in isolation, reveals that the early-type dwarfs in galaxy clusters need not be harassed or tidally stirred spiral galaxies.

Key words: galaxies: dwarf – galaxies: elliptical and lenticular, cD – galaxies: evolution – galaxies: formation – galaxies: kinematics and dynamics.

1 INTRODUCTION

Early-type dwarf galaxies (dE/dS0s) are the dominant galaxy type in galaxy clusters but are rare in the field (Binggeli, Sandage & Tammann 1988). The prevalent conclusion is that a high-density environment is essential for their formation. Early-type dwarfs are characterized by B -band luminosity fainter than $M_B > -18 \text{ mag}$ ($M_r > -19.3 \text{ mag}$), corresponding to stellar masses below $M_* < 5 \times 10^9 M_\odot$, early-type morphology and a predominantly quenched stellar population. Some of them exhibit features usually connected to discs, such as spiral arms and bars, as well as other morphological signs of a disc (Binggeli & Cameron 1991; Jerjen, Kalnajs & Binggeli 2000; Barazza, Binggeli & Jerjen 2002; de Rijcke et al. 2003; Geha, Guhathakurta & van der Marel 2003; Graham & Guzmán 2003; Lisker, Grebel & Binggeli 2006a; Penny et al. 2014). Their average shape is typical of a thick disc (Sánchez-Janssen, Méndez-Abreu & Aguerri 2010). Often these features are

thought to be inherited from a disc-like progenitor. While it is debated whether structural decompositions can be used to support or constrain such a transformation scenario (Aguerre et al. 2005; Janz et al. 2012, 2014; Aguerri 2016), the significant rotational component found in the kinematics of several early-type dwarfs (e.g. Pedraz et al. 2002; Geha et al. 2003, and many others since then) is sometimes understood as direct evidence for them being the remnants of spiral or irregular disc galaxies, which were transformed by the high-density environment.

Physical processes that are thought to explain such transformations via gas removal and dynamical heating unavoidably act in these environments due to the presence of hot gas, a high density of galaxies and deep potential wells (i.e. ram pressure stripping and harassment; Gunn & Gott 1972; Moore et al. 1996). Recently, a large fraction of dwarf galaxies in the Virgo cluster were shown to be rotating (Toloba et al. 2015). Similarly, Penny et al. (2016) found that the majority of quenched dwarfs in the first year of data from the Mapping Nearby Galaxies at APO (MaNGA) survey are also rotating, and many have disc-like morphologies. This raises the question whether all early-type dwarfs in galaxy clusters are transformed discs.

* Email: joachim.janz@gmail.com

While early-type dwarfs in the field are rare, they do still exist (e.g. Gu et al. 2006). The finding that such galaxies rotate will invalidate the conclusion that rotating early-type dwarfs necessarily were spiral galaxies that were then transformed by the cluster environment. In fact, for the early-type dwarfs in clusters, it has been suggested that only the combination of several different processes can explain the varied properties of early-type dwarfs (see, e.g., Lisker 2009, for an overview). These include the aforementioned ram pressure stripping and harassment, but also starvation and tidal stirring (e.g. Mayer et al. 2001; Boselli et al. 2008).

Another alternative (e.g. de Rijcke et al. 2005; Janz & Lisker 2008, 2009) to the harassment of (more massive) disc galaxies is particularly relevant when considering the quenched low-mass objects in low-density environments or isolation. In the Λ cold dark matter model of the Universe, low-mass dwarf galaxies are the first galaxies to form. These semi-pressure-supported systems are the building blocks of massive galaxies in a hierarchically assembling Universe. They may have preferentially formed in overdense regions that became galaxy groups and clusters.

More massive early-type galaxies often contain a significant rotating disc (e.g. ATLAS^{3D}, Emsellem et al. 2011; Scott et al. 2014, and references therein; SLUGGS, Arnold et al. 2014; Foster et al. 2016). None the less, not all of these galaxies are thought to be transformed spirals. This already indicates that the presence of a rotating disc in early-type galaxies is not necessarily conclusive for a (more massive) spiral progenitor. Like these higher mass early-type galaxies, some early-type dwarfs too may have acquired a disc around a pre-existing, possibly pressure-supported, (lower mass) progenitor (e.g. Graham, Dullo & Savorgnan 2015, and references therein), may have continuously grown from a fainter disc (Tadaki et al. 2017) or may just have formed in a dissipate collapse (e.g. Naab et al. 2014) to become dwarf lenticular (dS0) galaxies.

In this study, we present a systematic search for isolated quenched low-mass galaxies (Section 2), which allowed us to select suitable candidates for follow-up spectroscopy (Section 3). The data analysis is described in Section 4, and in Section 5 we characterize the kinematics of our objects and compare them to those of early-type dwarfs in the Virgo cluster. Possible ways to form isolated galaxies like those in our sample are discussed in Section 6. Moreover, the important implications of our findings of rotating quenched low-mass galaxies in isolation for the formation scenarios of early-type dwarfs in clusters are highlighted in this section.

2 SAMPLE SELECTION

We seek to identify low-mass galaxies in the Local Universe that are quenched and located in very low density environments. Geha, Blanton, Yan & Tinker (2012) searched for isolated quenched galaxies and found none below a stellar mass of $M_* < 10^9 M_\odot$, but more than 300 with a stellar mass of $10^9 M_\odot < M_* < 10^{10} M_\odot$. Following their methodology, we search for quenched galaxies in the mass regime of dwarf galaxies without a close bright neighbour. The data and our selection criteria are described below.

The large data volume of the Sloan Digital Sky Survey (SDSS; Eisenstein et al. 2011) spectroscopic sample is utilized and queried via the NASA-Sloan Atlas.¹ Distances are calculated based on the recession velocities and assuming a Hubble flow (throughout our analysis we use $H_0 = 70 \text{ km s}^{-1} \text{ Mpc}^{-1}$, $\Omega_m = 0.3$, $\Omega_\Lambda = 0.7$). Our

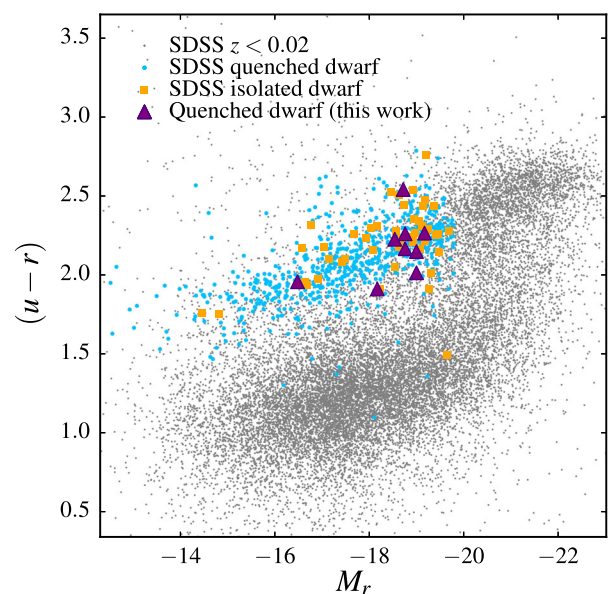


Figure 1. Colour–magnitude diagram for galaxies in the NASA-Sloan Atlas with $z < 0.02$ ($D \sim 86 \text{ Mpc}$). Objects with lower redshift ($z < 0.005$) have been excluded from the plot. Quenched dwarf galaxies in all environments with $M_B > -18 \text{ mag}$ are shown as blue points, and those dwarfs with a projected separation $D_{\text{proj}} > 1 \text{ Mpc}$ from their nearest bright neighbour within a velocity interval of 500 km s^{-1} are shown as orange squares. Our Keck ESI targets are shown as purple triangles. All targets fall on the galaxy red sequence.

search covers $z < 0.02$, comparable to the distance of the Coma cluster ($z = 0.0231$; $D = 100 \text{ Mpc}$). At the SDSS spectroscopic limit $r_{\text{Petrosian}} = 17.77 \text{ mag}$ for galaxies, all targets at $z = 0.02$ with spectroscopic redshifts will be brighter than $M_r = -17.11 \text{ mag}$. Generally, the completeness will vary as a function of the position in sky and local galaxy density, but is better for less crowded fields. To restrict the sample to low-mass galaxies, an upper stellar mass cut of $M_* < 2.45 \times 10^9 M_\odot$ as listed in the NASA-Sloan Atlas was applied, corresponding to $M_* < 5 \times 10^9 M_\odot$ using $H_0 = 70 \text{ km s}^{-1} \text{ Mpc}^{-1}$ (the NASA-Sloan Atlas employed $H_0 = 100 \text{ km s}^{-1} \text{ Mpc}^{-1}$). The central velocity dispersions were required to be smaller than $\sigma < 100 \text{ km s}^{-1}$, consistent with dwarf galaxies previously examined in the literature. This selects Large Magellanic Cloud mass and lower (see Penny et al. 2016). All candidates in the final sample have B -band magnitudes of $M_B \gtrsim -18 \text{ mag}$, the classical demarcation line between normal and dwarf galaxies (e.g. Ferguson & Binggeli 1994).

To identify quenched objects, we followed the prescription of Geha et al. (2012), selecting galaxies with a strong 4000 \AA break, $D_n(4000) > 0.6 + 0.1 \times \log_{10}(M_*/M_\odot)$, and little or no $\text{H}\alpha$ emission, with equivalent widths $\text{EW}_{\text{H}\alpha} < 2 \text{ \AA}$. This requirement is met by 665 galaxies with a redshift of $z < 0.02$, which lie on the red sequence (Fig. 1). We note that we did not apply any morphological criterion, but this procedure effectively removed late-type, dwarf irregular galaxies. However, our selection criteria exclude a number of early-type dwarfs with blue cores, e.g. objects like those in the Virgo cluster classified as dE(bc) by Lisker, Glatt, Westera & Grebel (2006b). The NASA-Sloan Atlas contains 31 of their 38 dE(bc)s, and 16 of them were excluded by our sample selection since they have $\text{EW}_{\text{H}\alpha} > 2 \text{ \AA}$. We note that this potentially excludes a higher fraction of early-type dwarfs in less dense environments, since these

¹ <http://www.nsatlas.org>

typically have blue cores and residual star formation (e.g. Tully & Trentham 2008; Pak et al. 2014). LEDA 2108986 (Graham et al. 2017) was initially excluded at this stage, since it did not meet the limit in $H\alpha$ equivalent width ($EW_{H\alpha} > 2 \text{ \AA}$). We include this galaxy here, since it is well isolated ($D_{\text{proj}} = 3.33 \text{ Mpc}$), has a strong 4000 \AA break $D_n(4000) = 1.24$, is rather faint ($M_B = -16.96 \text{ mag}$) and has early-type morphology. Galaxies with clear signs of spiral structures, an AGN, and star formation in the outer regions (which was missed by the SDSS fibre), along with any satellite trails, were manually removed after a visual inspection of their SDSS colour imaging. All galaxies finally selected for spectroscopy are of smooth appearance devoid of irregularities and mostly quite featureless.

From this sample of quenched low-mass galaxies, we select those galaxies that are well separated ($D_{\text{proj}} \gtrsim 1 \text{ Mpc}$) from massive neighbours (Table 1). Both the SDSS and the 2MASS redshift survey (Huchra et al. 2012) were queried for bright neighbours with $M_{K_s} < -23 \text{ mag}$ (see Geha et al. 2012; corresponding to $M_* \gtrsim 3 \times 10^{10} M_\odot$ when assuming a K_s -band mass-to-light ratio of unity) within a velocity interval of $\pm 500 \text{ km s}^{-1}$ around the recession velocity of each low-mass galaxy. The projected distance between the quenched dwarfs and their nearest bright neighbour was converted to a physical scale assuming the distance of the dwarf given by its recession velocity. These restrictions are slightly less restrictive than those criteria for isolation used by Geha et al. (2012). We discuss the differences, and also a more restrictive choice of the massive neighbour luminosity ($M_{K_s} < -21.5 \text{ mag}$) in Section 6.1.

The closest neighbour distance limit excluded the majority of quenched low-mass galaxies (mean projected separation to nearest bright neighbour $D_{\text{proj}} = 0.36 \text{ Mpc}$; Fig. 2), which are located in groups and clusters, and resulted in a sample of 46 candidates of isolated, quenched dwarf galaxies (highlighted as blue points in Fig. 1). The median distance in projection to the closest bright neighbour beyond 1 Mpc for this sample is 1.85 Mpc, and the median velocity difference relating to that neighbour is $|\Delta V| = 222 \text{ km s}^{-1}$.

From this sample, suitable targets were chosen so that their surface brightness allowed us to measure extended rotation curves with reasonable integration times, and that the observations were not hampered by bright foreground or background objects. For comparison, we also calculate their stellar masses from the absolute r -band magnitudes, assuming a mean stellar age of 5 Gyr (comparable to quenched dwarfs in the Virgo cluster; see Toloba et al. 2014a), $[\text{Fe}/\text{H}] = -0.33$ and a Kroupa initial mass function (see Table 1). The median stellar mass for the spectroscopic sample is $M_* \sim 4 \times 10^9 M_\odot$. Fig. 3 shows the nine galaxies (upper part of Table 1) for which we obtained spectra.

We note that one of our targets (CGCG038-085) was classified as a member of a galaxy group by Berlind et al. (2006) and has a neighbouring galaxy with an angular separation of 48 arcsec corresponding to 36 kpc at the group distance. The recession velocity of the target listed by the NASA/IPAC Extragalactic Database suggests that it is a group member. However, the SDSS spectrum and our analysis place the object clearly in the foreground with respect to the group ($\Delta V > 7000 \text{ km s}^{-1}$ with a velocity dispersion of the group of 57 km s^{-1}). Fuse, Marcum & Fanelli (2012) list VIII Zw040 and LEDA 2108986 as extremely isolated early-type galaxies. The study mentions two companion galaxies fainter than $M_V = -16.5 \text{ mag}$ for the latter. While we could not determine with certainty which galaxies were meant, we found the two nearest neighbours (with $M_r = -15.28$ and -15.78 mag) to be well

separated with projected distances of 2.0 and 2.1 Mpc, respectively. Other galaxies with smaller angular separations are in background. CGCG101-026, LEDA 2108986 and VIII Zw040 are also listed as isolated galaxies by Argudo-Fernández et al. (2015), with separations from their closest neighbour of 2.01, 2.03 and 2.41 Mpc, respectively. In these cases, the closest neighbouring galaxies are fainter than our limiting magnitude of $M_{K_s} < -23 \text{ mag}$.

3 DATA

We observed nine of the quenched, isolated low-mass galaxies (Table 1) with the Echellette Spectrograph and Imager (ESI; Sheinis et al. 2002) on the Keck II telescope on 2016 January 11 and 2016 March 14. ESI was used in the echellette mode with a slit width of 0.75 arcsec. This setup results in a spectral coverage of ~ 4000 to $10\,000 \text{ \AA}$ across 10 echelle orders, and a velocity resolution of $\sigma \sim 25 \text{ km s}^{-1}$. The galaxy centre was put in the middle of the slit that was aligned with the galaxy's major axis. The integrations for each object were split into at least three individual exposures. Total exposure times, position angles and observing conditions are summarized in Table 2. Furthermore, we obtained several stellar spectra with the same setup. In each run, we observed one star to trace the echelle orders in the reduction process, as well as velocity standards to be used as templates for measuring the kinematics. This template library was augmented by spectra of velocity standards from previous runs so that our stellar library comprises in total 16 standards, spanning spectral types from O9V to K7V with a range of metallicities and containing larger numbers of standards for the later spectral types.

We prepared master frames of the necessary calibrations (internal flat-fields, bias, arc lamps) by combining the two-dimensional spectra with the `imcombine` task in IRAF. The subsequent data reduction was then carried out with MAKEE.² The pipeline subtracts the bias from the science spectra and divides them by the flat-field. It traces the echelle orders with a bright trace star and extracts one-dimensional spectra for each order in spatial apertures that can be defined by the user.

To obtain spatially resolved kinematics, we extracted spectra from apertures with a width of 0.9 arcsec along the slit, which corresponds to the average full width at half-maximum (FWHM) of the seeing. The first extraction is centred on the galaxy, while the next ones were extracted from increasingly larger radii to both sides. The largest angular extent was probed for 2MASX J08192430, for which we extracted five spectra on each side of the central spectrum. In this case, the apertures furthest away from the galaxy centre are twice as wide as the other to improve the signal-to-noise (S/N).

The spectra were wavelength calibrated using the known emission lines of the arc lamps and the night sky. The pixel uncertainties were calculated for each of the spectra. Finally, the extracted spectra from individual exposures were co-added for each aperture in a S/N optimized manner, with a minimum final signal-to-noise of $S/N \gtrsim 7 \text{ \AA}^{-1}$ being required for consideration further analysis. We display the spectra in the Ca II triplet spectral region of the central extraction for each of the galaxies in Fig. 4.

SDSS images are available for all of the targets. We used the background-subtracted, calibrated images (see Fig. 3) of data release DR12 (Alam et al. 2015) for the photometry and other imaging-based measurements (see the next section).

² Written by T. Barlow, <http://www2.keck.hawaii.edu/inst/esi/makee.html>.

Table 1. Sample of isolated quenched low-mass galaxies.

Galaxy	PGC	RA	Dec.	Type	$M_{B, \text{tot}}$	$\log_{10}(M_*/M_\odot)$	Closest luminous neighbour			
							D_{500}	$ \Delta V_{500} $	D_{1000}	$ \Delta V_{1000} $
		(h:m:s)	($^{\circ}$: $'$: $''$)		(mag)		(Mpc)	(km s $^{-1}$)	(Mpc)	(km s $^{-1}$)
LEDA 3115955	3115955	02:05:46.37	+00:37:33.8	E	-18.10 ± 0.35	9.73	1.67	13		
2MASX J03190758+4232179	2200915	03:19:07.58	+42:32:17.9	–	-17.41 ± 0.34	9.43	0.94	130		
LCSBS1123P	1719550	08:17:15.93	+24:53:56.8	E	-15.17 ± 0.27	8.61	1.17	152		
2MASX J08192430+2100125	23346	08:19:24.30	+21:00:12.5	E?	-17.51 ± 0.41	9.75	1.00	314	0.11	987
VIII Zw 040	25889	09:11:05.58	+09:20:58.5	E(R)	-17.63 ± 0.37	9.52	3.78	455		
CGCG038-085	33187	11:00:41.76	+04:07:29.6	E	-17.73 ± 0.40	9.63	2.03	75		
2MASX J11521124+0421239	1267103	11:52:11.24	+04:21:23.9	E	-17.62 ± 0.43	9.58	4.48	292	1.38	662
CGCG101-026	46516	13:20:06.92	+14:32:35.7	ES0	-18.04 ± 0.25	9.68	2.40	263		
LEDA 2108986	2108986	15:03:15.57	+37:45:57.2	ES0	-16.96 ± 0.38	9.24	3.07	21		
J001212.41–110010.4	3099480	00:12:12.41	–11:00:10.4	–	-16.04 ± 0.36	8.77	3.71	387	1.51	509
J001530.03+160429.7	1500123	00:15:30.03	+16:04:29.7	–	-15.91 ± 0.40	8.91	1.63	211		
J001601.19+160133.4	212493	00:16:01.19	+16:01:33.4	Sb	-17.67 ± 0.45	9.62	1.76	41		
J012506.69–000807.0	4131836	01:25:06.69	–00:08:07.0	–	-15.58 ± 0.39	8.67	1.35	31		
J013842.89–002053.0	1145615	01:38:42.89	–00:20:53.0	E	-16.75 ± 0.40	9.15	1.54	87		
J045058.77+261313.7	1767757	04:50:58.77	+26:13:13.7	–	-15.82 ± 0.40	9.84	1.94	280	1.83	661
J075303.96+524435.8	3724966	07:53:03.96	+52:44:35.8	E	-17.21 ± 0.50	9.38	1.04	63		
J082013.92+302503.0	1902931	08:20:13.92	+30:25:03.0	E	-17.23 ± 0.35	9.37	2.94	102		
J082210.66+210507.5	1642425	08:22:10.66	+21:05:07.5	–	-15.40 ± 0.41	8.72	1.02	453	0.36	551
J084915.01+191127.3	4572078	08:49:15.01	+19:11:27.3	–	-15.67 ± 0.29	8.59	3.72	373	0.11	526
J085652.63+475923.8	2308331	08:56:52.63	+47:59:23.8	E	-17.29 ± 0.34	9.34	3.67	277		
J091514.45+581200.3	26096	09:15:14.45	+58:12:00.3	E	-17.66 ± 0.38	9.57	6.90	350	3.61	714
J091657.98+064254.2	3456113	09:16:57.98	+06:42:54.2	E	-17.55 ± 0.35	9.52	2.56	211		
J093016.38+233727.9	1690666	09:30:16.38	+23:37:27.9	E	-16.83 ± 0.28	9.19	2.27	416		
J093251.11+314145.0	3743536	09:32:51.11	+31:41:45.0	E	-17.74 ± 0.35	9.52	3.30	191		
J094408.52+111514.8	3531658	09:44:08.52	+11:15:14.8	Sb	-17.91 ± 0.35	9.63	2.77	320	0.34	922
J094834.50+145356.6	1469954	09:48:34.50	+14:53:56.6	E	-17.80 ± 0.59	9.84	1.41	6		
J100003.93+044845.0	1273634	10:00:03.93	+04:48:45.0	E	-15.76 ± 0.37	8.88	1.24	80		
J105005.53+655015.6	3097669	10:50:05.53	+65:50:15.6	E	-16.68 ± 0.30	9.01	5.66	400		
J110423.34+195501.5	3765330	11:04:23.34	+19:55:01.5	E	-15.43 ± 0.35	8.62	1.07	11		
J112422.89+385833.3	4098131	11:24:22.89	+38:58:33.3	–	-12.94 ± 0.50	7.87	1.30	354	0.06	925
J114423.13+163304.5	213877	11:44:23.13	+16:33:04.5	E	-17.88 ± 0.37	9.71	1.47	386	0.02	549
J120300.94+025011.0	1238733	12:03:00.94	+02:50:11.0	E	-17.46 ± 0.52	9.72	1.06	55		
J120823.99+435212.4	2231154	12:08:23.99	+43:52:12.4	E	-17.61 ± 0.32	9.66	4.42	230		
J122543.23+042505.4	1267954	12:25:43.23	+04:25:05.4	Sb	-17.80 ± 0.38	9.66	3.24	261	2.08	804
J124408.62+252458.2	1735700	12:44:08.62	+25:24:58.2	E	-17.61 ± 0.49	9.62	1.11	421		
J125026.61+264407.1	1786738	12:50:26.61	+26:44:07.1	E	-16.72 ± 0.31	9.04	1.05	353		
J125103.34+262644.6	94058	12:51:03.34	+26:26:44.6	E	-17.61 ± 0.30	9.46	1.21	180		
J125321.68+262141.1	1773332	12:53:21.68	+26:21:41.1	Sc	-17.54 ± 0.38	9.40	1.05	382		
J125756.52+272256.2	126848	12:57:56.52	+27:22:56.2	E	-16.58 ± 0.29	9.12	1.17	215	0.32	836
J125940.10+275117.7	44654	12:59:40.10	+27:51:17.7	S0a	-16.94 ± 0.29	9.45	4.20	123	0.23	790
J130320.35+175909.7	4352778	13:03:20.35	+17:59:09.7	E	-13.05 ± 0.02	7.73	1.04	164	0.96	553
J130549.09+262551.6	1775990	13:05:49.09	+26:25:51.6	E	-16.95 ± 0.31	9.22	2.02	39		
J142914.46+444156.3	51753	14:29:14.46	+44:41:56.3	S0	-17.81 ± 0.28	9.60	2.51	243		
J144621.10+342214.1	52741	14:46:21.10	+34:22:14.1	S0	-17.58 ± 0.32	9.63	6.25	460	3.89	926
J160810.70+313055.0	1950976	16:08:10.70	+31:30:55.0	E	-17.74 ± 0.41	9.55	5.52	72		
J232028.21+150420.8	1474455	23:20:28.21	+15:04:20.8	–	-17.61 ± 0.34	9.53	1.02	438	0.84	559

Notes. The first four columns list the galaxy name (for the objects with the 2MASX designation, we use abridged versions of the name throughout the paper), its number in the PGC and its coordinates (equinox J2000). The galaxy classifications (column 5) and total B -band magnitudes (column 6; extinction corrected) are from HyperLeda. The distances for the absolute magnitudes are calculated using the recession velocities (from SDSS and our updated values for the galaxies above the line). Column 7 lists the stellar mass (see the text). The closest bright neighbour within a velocity interval of $\pm 500 \text{ km s}^{-1}$ is extracted from a combined catalogue containing redshifts from the NASA-Sloan Atlas and the 2MASS redshift survey. The projected (linear) distance between the neighbour and the low-mass galaxy and the difference between their recession velocities are given in columns 8 and 9. If there is an additional closer neighbour within a velocity interval of $\pm 1000 \text{ km s}^{-1}$, the corresponding details are listed in columns 10 and 11. Keck ESI spectroscopy is presented for the galaxies above the line in Section 4.2.

4 ANALYSIS

4.1 Imaging-based quantities

For our analysis, we need measurements of the brightnesses, colours, sizes and ellipticities of the galaxies. These were obtained

by analysing SDSS images as provided by the DR12 pipeline and by querying the SDSS data base. More details are given in the following paragraphs.

For the photometric and size measurements in the r -band images, we followed an approach similar to Janz & Lisker (2008).

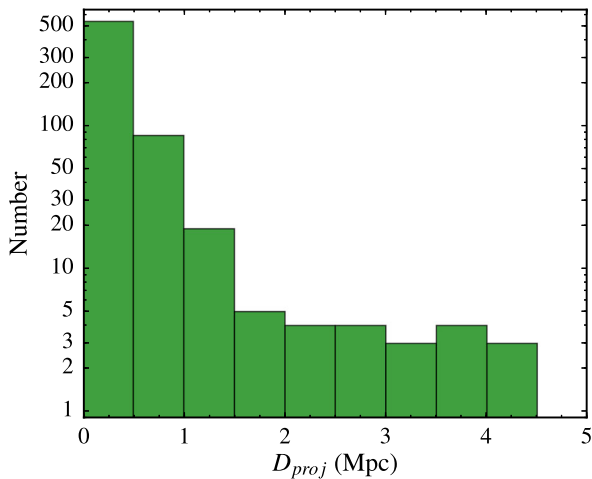


Figure 2. Histogram showing the projected separation of each quenched dwarf in the NASA-Sloan Atlas with $z < 0.02$ (blue points in Fig. 1) from a luminous galaxy with $M_{K_s} < -23$ mag ($M_* \gtrsim 3 \times 10^{10} M_\odot$) within a velocity interval of $\pm 500 \text{ km s}^{-1}$. The majority of dwarfs are located at small separations from a nearby luminous galaxy, with a mean projected separation $D_{\text{proj}} = 0.36 \text{ Mpc}$.

First, the elliptical Petrosian aperture, i.e. the ellipse at which the isophotal intensity drops to 0.2 times the average intensity within that aperture, was determined. Secondly, the flux, and the semi-major axis containing half that flux (a_{50} , for which we use the notation R_e hereafter), was measured within an aperture with twice the Petrosian semi-major axis. Those values were corrected for flux missed by this aperture using concentration measures and the formulae provided in Graham et al. (2005). The fluxes were corrected for Galactic extinction (Schlegel, Finkbeiner & Davis 1998, as provided by the SDSS data base), and converted to absolute magnitudes based on the distances determined as detailed below.

These size measurements systematically differ from those (circular) Petrosian R_{50} listed in the SDSS data base. In order to test the reliability, and to verify our sizes, we also fit Sérsic models to the galaxies with GALFIT (Peng, Ho, Impey & Rix 2010) using models for the point spread function (PSF) created with SExtractor (Bertin & Arnouts 1996) and PSFEX (Bertin 2011). The non-parametric size measurements and the half-light radii from the Sérsic model fits are consistent with each other with an average deviation of 6 per cent (when disregarding two galaxies, which were not well fitted with this model, resulting in $n > 4$; e.g. because of a two-component structure). For the further analysis, the non-parametric measurements are adopted.

The ellipticities are calculated from the adaptive image moments in the i band (which has the smallest FWHM), provided by the SDSS pipeline, taking into account the PSF (see Bernstein & Jarvis 2002). These ellipticities agree with those from the Sérsic model fits to the r -band images (also taking the PSF into account) within 12 per cent (excluding one further outlier, 2MASX J03190758, for which the deviation is due to radial variations of the ellipticity). Both ellipticity measurements are light-weighted so that they are a proxy for the light-weighted average ellipticity within R_e . For the ellipticities, we also adopt the non-parametric measurements. We also ran the IRAF ellipse task to measure the ellipticities at R_e for comparison. For

all but two galaxies, these ellipticities were compatible within the uncertainties with those that we adopted.³

Finally, $g - i$ colours are obtained for the sake of a comparison with the sample of Virgo early-type dwarfs. For that, we queried the SDSS catalogue for 7 arcsec aperture colours and corrected them for Galactic reddening. The measurements described in this section are summarized in Table 3.

4.2 Kinematics

The recession velocity and velocity dispersion are determined with ppxf (Cappellari & Emsellem 2004). The code simultaneously determines the velocity shift and broadening by velocity dispersion, while finding the best-fitting template as a linear combination of the spectra in the template library by using a penalized pixel-fitting method. In our case, the library consists of velocity standard stars observed with the same setup.

For the fitting, two spectral ranges in different echelle orders with a number of metal absorption features are used. These were the ranges containing the Mg b and Ca II triplets ($5100 \text{ \AA} < \lambda < 5400 \text{ \AA}$ and $8480 \text{ \AA} < \lambda < 8710 \text{ \AA}$ in the rest frame), both of which also contain several weaker iron absorption lines. In order to obtain estimates for the uncertainties, we ran Monte Carlo simulations of the fitting process by altering the observed spectra by addition of Gaussian noise according to their pixel uncertainties. The final values for the velocities and the central velocity dispersions are the weighted averages (with the inverse variance of the individual values) from the fits in the two independently fitted spectral regions. The uncertainties of these values take into account those of the individual measurements as well as discrepancies between them by quadratically adding them (for the velocities: in Table 4 the difference between the Mg and Ca, while in the rotation curves just the difference of the shifted values). The spectra and ppxf fits for the central apertures for the Ca II triplet are displayed in Fig. 4.

In all galaxies, we required the extracted spectrum of each aperture to have $S/N \gtrsim 7 \text{ \AA}^{-1}$ for the velocity information to be considered in the further analysis. Furthermore, the two independently fitted spectral ranges had to yield consistent results. Small systematic offsets in the velocities between the two spectral ranges were subtracted by determining the offset from the weighted average for each of them in the central aperture with the highest S/N . The central aperture was also used to derive the central velocity dispersion σ_{cen} . Geha, Guhathakurta & van der Marel (2002) found that it is feasible to reliably measure (with an accuracy of 1 per cent) velocity dispersions at the instrumental resolution with a similar setup and $S/N = 10 \text{ pixel}^{-1}$ (and with an accuracy of 10 per cent down to $\sigma \sim 18.5 \text{ km s}^{-1}$).

We qualitatively confirm this σ limit for our ESI instrumental setup with our own idealized Monte Carlo simulation to determine the minimum velocity dispersion that can be recovered by ppxf. One of our spectroscopic standard stars, HR1015, which was observed using an identical instrumental setup to our target galaxies, is used as a mock galaxy spectrum for this simulation. To simulate an observed

³ The exceptions LEDA 3115955 and 2MASX J08192430 (with ellipticities at R_e of ~ 0.29 and 0.61 , respectively) are shifted in the v/σ and λ versus ellipticity diagrams in Section 5 when these ellipticities are used, but this does not change the conclusions. We also note that the comparison sample uses the average ellipticities within R_e .

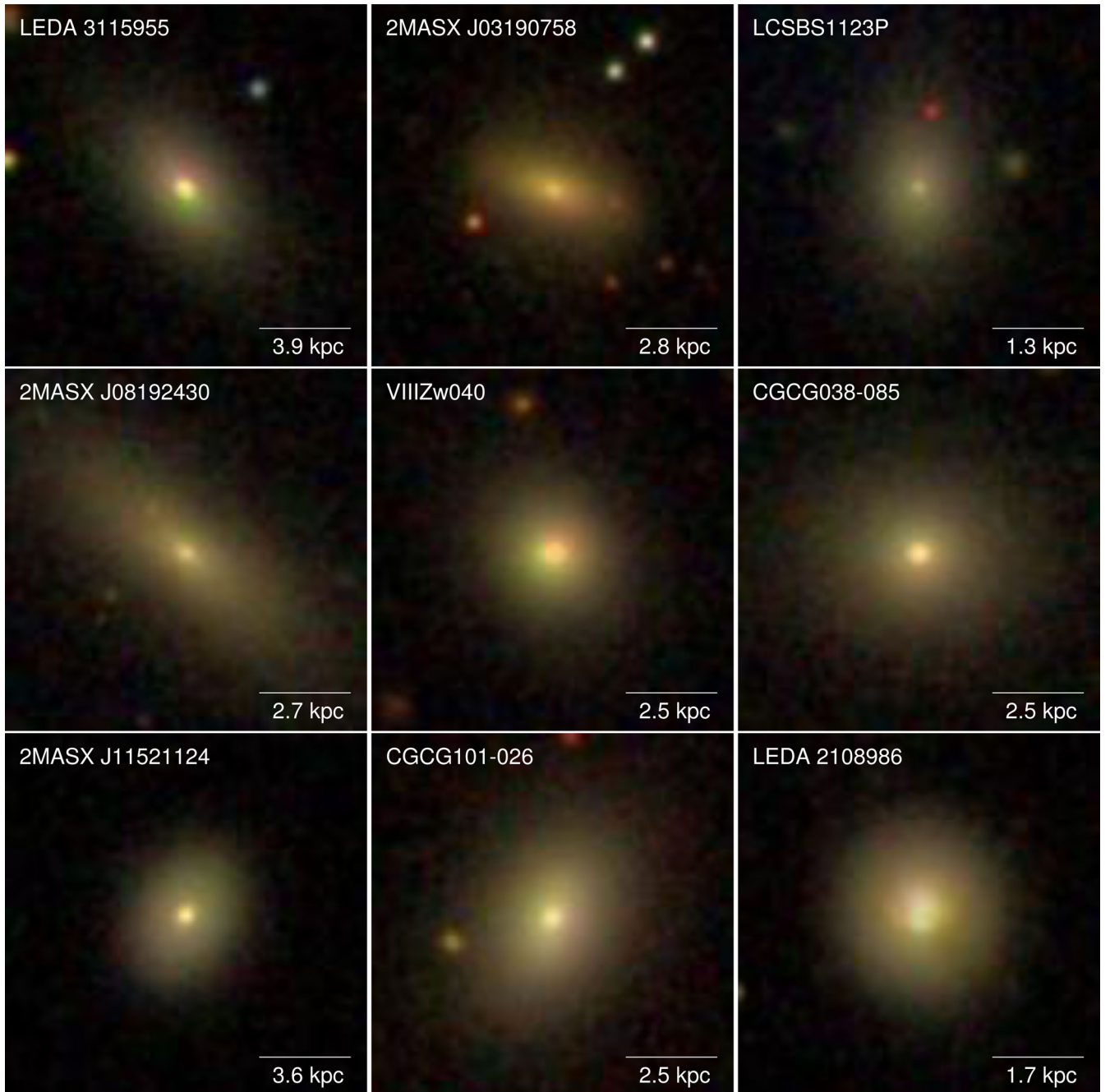


Figure 3. SDSS *r*-band images of the galaxies in our spectroscopic sample. An angular scale of 10 arcsec is provided in the lower-right corner of each panel together with the corresponding physical scale. North is up and east is left.

galaxy, this simulation takes this high- S/N standard star spectrum and oversamples it by a factor of 10. This oversampled template is then convolved with 1000 different values of σ_{test} between 5 and 100 km s^{-1} , to simulate galaxies with different velocity dispersion. The simulation then adds noise to the oversampled spectrum until the required S/N per original pixel is met. This broadened, noise added, normally sampled spectrum is then used as a mock galaxy spectrum, with the original, high- S/N , unbroadened spectrum used as a template by `pPXF` (i.e. the simulation does not take into account possibly template mismatches). `pPXF` is then run to test how well

the artificial velocity broadening was recovered. The results of this simulation are shown in Fig. 5 for four different S/N ratios (10, 20, 30 and 50 pixel^{-1}).

The spectra in the central apertures have at least $S/N \geq 10 \text{ pixel}^{-1}$, in both spectral ranges (in most cases larger by some), for all our observations, and we note that all the measured central velocity dispersions exceed the instrumental resolution ($\sigma_{\text{instr}} \sim 25 \text{ km s}^{-1}$), and are thus reliable. We also note that the central velocity dispersions are consistent within the errors with those listed in the SDSS data base for all galaxies but those with the most significant rotation

Table 2. Observing log.

Galaxy	Run	Exp. time (min)	PA (deg)	Seeing (arcsec)
LEDA 3115955	15B	90	39	1.0
2MASX J03190758	15B	60	72	0.9
LCSBS1123P	15B	120	178	1.1
2MASX J08192430	15B	90	50	0.8
VIII Zw040	16A	40	14	0.8
CGCG038-085	16A	120	84	0.7
2MASX J11521124	15B	90	156	0.8
CGCG101026	16A	60	159	0.9
LEDA 2108986	16A	75	158	0.8

Notes. The second column indicates during which run the spectra were taken, the third and fourth columns list the total integration time and the position angle of the slit (PA; east of north), while the fifth column gives the FWHM of the seeing. During the 16A run, the conditions were variable.

(see below). The higher values in SDSS in these cases reflect the larger spatial coverage of the SDSS fibre (3 and 2 arcsec for the SDSS and BOSS spectrographs, respectively).

4.3 Harmonization of kinematics

A comparison of the rotation curves for our sample, and ultimately with the kinematics of early-type dwarfs in the Virgo cluster, needs

to be carried out in a consistent way. The rotation curves, e.g. for exponential discs, are expected to be rising up to 2.2 scalelengths (Freeman 1970), i.e. beyond the typical extent of our measurements and those in the literature. Therefore, the rotation amplitude at a common radius is used. We chose the galaxy half-light radius R_e , as also done by Toloba et al. (2015) for the Virgo dwarfs.

Not all of our rotation curves reach R_e , nor do they uniformly sample the rotation amplitude at that radius, i.e. the apertures from which the spectra were extracted do not correspond to equal physical scales for different galaxies. For inter- and extrapolation of the rotation curves at R_e , we fit model rotation curves (Fig. 6) parametrized by the *Polyex* function suggested by Giovanelli & Haynes (2002):

$$V_{\text{poly}}(R) = V_0 \left\{ (1 - e^{-R/R_{\text{PE}}}) \times (1 + \alpha R/R_{\text{PE}}) \right\}, \quad (1)$$

with the rotation amplitude V_0 . The scalelength of the steep inner rise R_{PE} and the slope in the slowly varying outer parts α are not well constrained by our data with its radial limitations. Catinella, Giovanelli & Haynes (2006) fit *Polyex* models to a large number of rotation curves of disc galaxies and co-additions thereof, increasing the radial coverage to several exponential scalelengths h . They concluded for low-luminosity galaxies $\alpha \sim 0.02$ and $R_{\text{PE}} \sim h$. In our fits, we use these values as fixed parameters (with $h \approx 0.6 R_e$ for exponential profiles) leaving only the rotation amplitude as a free parameter. We note that the *Polyex* model is a versatile phenomenological model used for rotating discs and that we use the galactic size and we do not try to separate possibly embedded discs. This

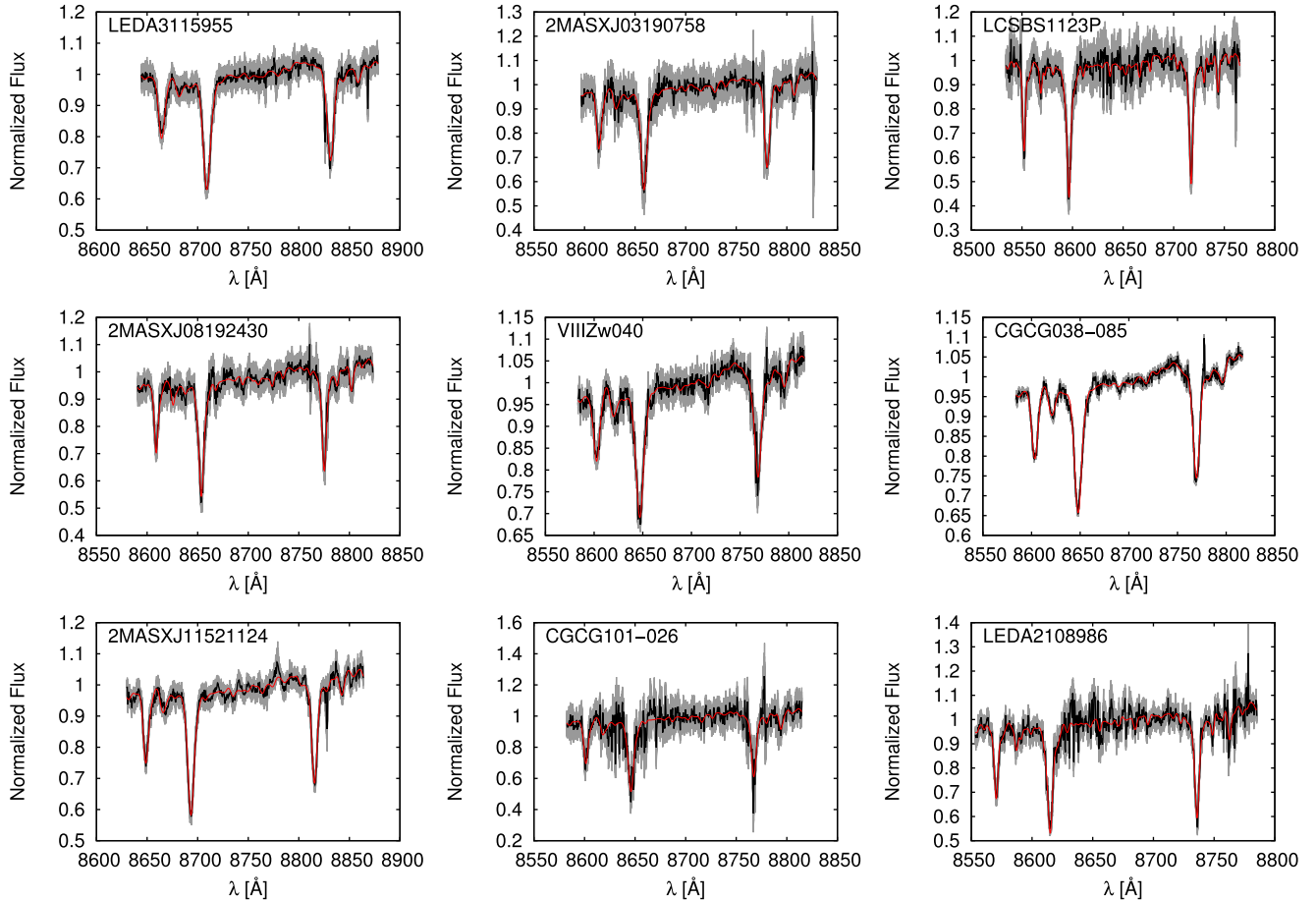


Figure 4. Spectra of the central aperture for all galaxies in the Ca II triplet spectral region. The black and red lines are the observed spectrum and the ppxf fit, respectively, while the Monte Carlo realizations of the observed spectra are plotted in grey.

Table 3. Photometry and other imaging measurements.

Galaxy	M_r (mag)	R_e (arcsec)	ϵ	$g - i$ (mag)
LEDA 3115955	-19.30	3.9	0.39	1.03
2MASX J03190758	-18.54	5.2	0.42	1.11
LCSBS1123P	-16.48	7.4	0.25	0.98
2MASX J08192430	-19.00	13.2	0.47	1.09
VIIIZw040	-18.72	2.6	0.07	1.12
CGCG038-085	-19.17	7.0	0.10	1.05
2MASX J11521124	-18.76	3.2	0.17	1.02
CGCG101-026	-19.00	4.4	0.29	0.99
LEDA 2108986	-18.17	3.4	0.11	1.04

Notes. The absolute magnitudes and half-light radii are listed in the second and third columns. The ellipticities (fourth column) are calculated from the SDSS (DR12; Alam et al. 2015) adaptive image moments in the i band (which has the PSF with smallest FWHM) and corrected for the PSF. The $g - i$ colours in the fifth column are 7 arcsec aperture colours from the SDSS corrected for Galactic reddening.

Table 4. Spectroscopic measurements.

Galaxy	V (km s ⁻¹)	D (Mpc)	σ_{cen} (km s ⁻¹)	$V_{\text{rot,e}}$ (km s ⁻¹)	$\langle\sigma\rangle_e$ (km s ⁻¹)
LEDA 3115955	5808 ± 11	83.0	88 ± 1	27 ± 2	89 ± 1
2MASX J03190758	4076 ± 27	58.2	64 ± 2	19 ± 3	64 ± 2
LCSBS1123P	1905 ± 7	27.2	28 ± 1	5 ± 1	29 ± 1
2MASX J08192430	3894 ± 14	55.6	51 ± 1	69 ± 4	60 ± 2
VIIIZw040	3662 ± 13	52.3	99 ± 3	1 ± 3	99 ± 3
CGCG038-085	3692 ± 8	52.8	94 ± 1	74 ± 13	100 ± 3
2MASX J11521124	5270 ± 13	75.3	69 ± 1	19 ± 3	70 ± 1
CGCG101-026	3627 ± 10	51.8	48 ± 3	49 ± 3	53 ± 3
LEDA 2108986	2546 ± 4	36.4	36 ± 2	8 ± 4	37 ± 2

Notes. The heliocentric recession velocities (second column) are used to calculate the distances in the third column, assuming a Hubble flow with $H_0 = 70 \text{ km s}^{-1} \text{ Mpc}^{-1}$. The recession velocities and central velocity dispersions (fourth column) are weighted means of the fits to the Ca II and Mg b triplet spectral regions, and the uncertainties give the statistical uncertainties (see the text). The fifth column lists the rotation velocity at R_e of the *Polyex* model with the asymptotic standard error estimate from the Levenberg-Marquardt fitting algorithm (for LEDA 2108986 the alternative model fit, shown with a green curve in Fig. 6, results in $V_{\text{rot,e}} = 18 \pm 1 \text{ km s}^{-1}$). The final column lists the integrated $\langle\sigma\rangle_e$ within R_e , assuming the *Polyex* rotation curve, a constant σ and a Sérsic index of the surface brightness profile of $n = 2$ along with the propagated uncertainties from $V_{\text{rot,e}}$ and σ_{cen} (see the text).

approach was also followed by Toloba et al. (2015), who confirmed the applicability of these approximations for the rotation curves of early-type dwarfs in their sample with larger radial extent. For these objects, Toloba et al. also compared the rotation amplitudes obtained from fits to the whole rotation curve with those from fits with an artificial restriction to $R < 0.6 R_e$. The good agreement suggests that our extrapolation of the rotation curves to R_e for those objects with less extent is reasonable.

The velocity dispersion profiles of early-type dwarf galaxies are generally flat (e.g. Geha et al. 2003; Chilingarian 2009; Forbes et al. 2011; Ryś, van de Ven & Falcón-Barroso 2014; Penny et al. 2015; Toloba et al. 2015 as expected for systems with low Sérsic n , see Graham & Colless 1997; Terzić & Graham 2005). The objects in our sample for which we can extract radial information of the velocity dispersion confirm this within the uncertainties. For the further analysis, we chose to use for all galaxies the velocity dispersion measured in the central aperture with the highest

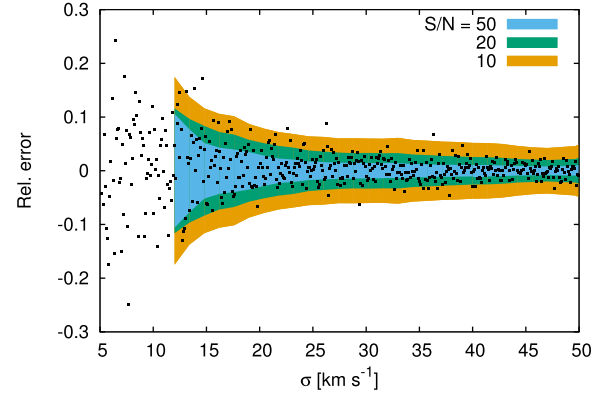


Figure 5. Relative error versus input σ for the Monte Carlo simulation described in Section 4.2. The contours are the 1σ scatter for the results of the $S/N = 50$ (blue), 20 (green) and 10 (orange) pixel⁻¹ runs, and the black points indicate the results for the simulation with $S/N = 30$ pixel⁻¹. Our central velocity dispersions with $S/N > 10$ have uncertainties smaller than 10 per cent.

S/N . We note that this would also be the dominating contributor, if the velocity dispersion was averaged over larger radial extent when weighting with the luminosity. The observed flat velocity dispersion profiles also suggest that the central value is not severely biased by the potentially different velocity dispersion of a nuclear star cluster (as, e.g., in NGC 205; Carter & Sadler 1990, see also Forbes et al. 2011).

When comparing rotation and random motions, we adopt a similar approach to Toloba et al. (2015). As described above, we quantify the rotation as the amplitude of the best-fitting *Polyex* model at R_e . The rotation is compared to a luminosity-weighted average of the second moment of the velocity field $\langle\sigma\rangle$ (with contributions from both the random motions and the rotation, see below). Toloba et al. (2015) achieved this by measuring the broadening of absorption lines on spectra, which were obtained by luminosity-weighted co-adding the spectra from within R_e on both sides of the galaxy centre. However, for finding the average broadening along the slit within $-R_e < R < +R_e$, we are limited by the radial extent of our observations. Instead of collapsing the spectra within such a large aperture, we calculated our values $\langle\sigma\rangle_e$ based on the *Polyex* model fits and the assumption that the velocity dispersion is independent of the radius (see above):

$$\langle\sigma\rangle_e^2 = \int_{-R_e}^{+R_e} V_{\text{poly}}^2(R) I(R) dR \bigg/ \int_{-R_e}^{+R_e} I(R) dR + \sigma_{\text{cen}}^2. \quad (2)$$

The relative contribution of the rotation to the luminosity-weighted average depends on the surface brightness profile. We numerically carry out the weighted average assuming different surface brightness profile shapes. For this, the surface brightness profile is parametrized by a Sérsic profile and we consider the cases with indices ranging from $n = 1$ to 4, a range that easily contains those indices expected for our galaxy sample. We list the averages for $n = 2$ and summarize all measurements described in this section in Table 4.

Furthermore, we calculate the spin parameter λ_e (Emsellem et al. 2007) in the following way, with

$$\lambda_{e,1D} = \sum_i F_i R_i |V_i| \bigg/ \sum_i F_i R_i \sqrt{V_i^2 + \sigma_i^2} \quad (3)$$

summing over several apertures along the slit within R_e , with the flux in an aperture F_i , its radial distance to the galaxy centre

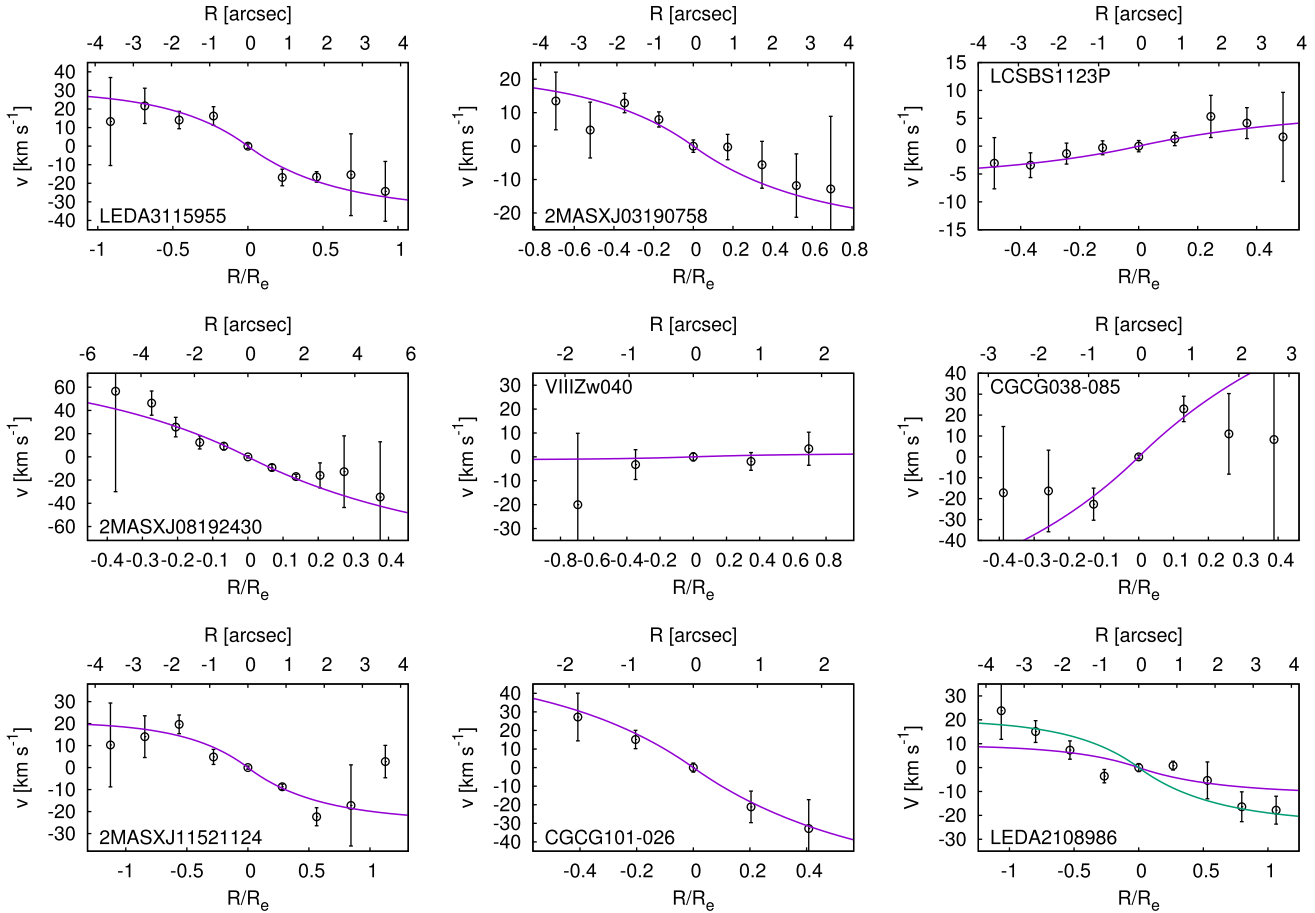


Figure 6. Rotation curves of galaxies in our sample. The uncertainties are from Monte Carlo simulations of the measurements and additionally take into account the consistency of the independent measurements for the two different spectral ranges used for fitting. The curves display fits of the *Polyx* model to the rotation curves (see the text). For LEDA 2108986, an alternative fit was obtained by disregarding the inner parts with a possibly distinct kinematic feature, and is shown as the green curve.

R_i , and its rotation velocity and velocity dispersion V_i and σ_i . Again, due to the unequal sampling of the rotation with small numbers of apertures, we base our λ_e calculation on the model rotation curve, the assumption of a spatially constant velocity dispersion and a Sérsic light profile [i.e. $V_i = V_{\text{poly}}(R_i)$, $\sigma_i = \sigma_{\text{cen}}$ and $F_i = F_e * \exp(-b_n[(\frac{R}{R_e})^{\frac{1}{n}} - 1])$, where the flux at the half-light radius F_e cancels out in the calculation of λ_e and we take a lower and upper extreme Sérsic index $n = 1$ and 4 to estimate its influence]. Toloba et al. (2015) applied a factor to convert the long-slit information to a value mimicking a measurement integrated over the whole half-light aperture, corresponding to what integral field spectroscopy would measure: $\lambda_e = 0.64 \lambda_{e, \text{ID}}$. This factor was determined from comparisons of modelled long-slit parameters and corresponding two-dimensional quantities using realistic velocity fields and surface brightness distributions (see Toloba et al. 2015). For maximal comparability, we employ the same factor.

5 RESULTS

We obtained rotation curves for nine isolated quenched low-mass galaxies (Fig. 6). For three galaxies, their extent is equal to or

exceeds R_e . For two galaxies, $\sim 0.7 R_e$ is reached, while for the remaining four $R_e/2$ is covered. In the following sections, we present the results in more detail and compare them to those for a sample of Virgo cluster dwarfs.

5.1 Variety of rotation profiles

At first we are interested in an internal comparison of the rotation curves within our sample. For that, we correct the rotation velocity for the inclination, which is estimated by the axial ratio, and normalize it to the central velocity dispersion, and likewise the radii to R_e (Fig. 7). Instead of a clear pattern arising, a range of different behaviours can be seen. There are rather rapidly rising curves, as well as very flat ones for objects that basically do not rotate.

Since this information is extracted from slit spectra, rotation could be missed when the rotation is misaligned with the major axis. Also, the slit could be misaligned when the position angle varies as a function of radius, or when the object is very round, which applies particularly to VIII Zw040. For this galaxy, however, its compactness and especially its high velocity dispersion suggest that it is genuinely dominated by random motions.

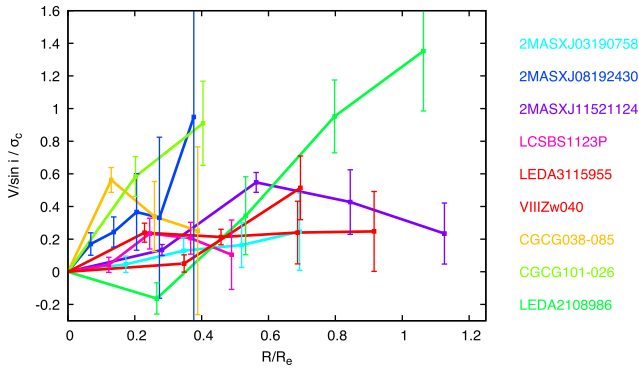


Figure 7. Rotation curves corrected for inclination (from ellipticity) and normalized by central velocity dispersion. The approaching and receding sides are folded together and averaged. A variety of different types of profiles can be seen.

The profiles of CGCG038-085, and possibly 2MASXJ11521124, are somewhat reminiscent of rotation curves of galaxies with bars (e.g. Sparke & Sellwood 1987; Bettoni 1989, and references therein). For CGCG038-085, there is a slight hint of a bar-like structure in the Sérsic model subtracted residual image. For LEDA 2108986, the innermost part of the rotation profile appears to be flat. This may hint at a kinematically decoupled core (KDC) with counter-rotating stars with respect to the outer motions. This claim is substantiated by counter-rotating ionized gas (rotating in alignment with a possible counter-rotating inner structure), which is discussed, along with an inner spiral structure, in a separate paper (Graham et al. 2016).

5.2 Comparison with Virgo cluster early-type dwarfs

Before comparing the internal kinematics of our galaxy sample to those of early-type dwarfs in the Virgo cluster, we consider other basic properties, i.e. colour–magnitude and size–magnitude relations (Fig. 8). The galaxies in our sample have on average somewhat brighter absolute r -band magnitudes compared to those in the Toloba et al. (2014a) comparison sample. This is also reflected in the velocity dispersions, which are larger than the largest dispersion in the Toloba et al. (2014a) sample for five of the galaxies in our sample.

The faintest galaxies in both samples are of similar absolute brightness. Consistent with the selection as quenched galaxies, the galaxies in our sample fall on the red sequence traced by the Virgo early types (Janz & Lisker 2009). It is noteworthy that their sizes span most of the size range of the Virgo early-type dwarfs (Janz & Lisker 2008), and their range of sizes exceeds that of the Toloba et al. (2014a) sample.

Toloba et al. (2015) found a similar variety of rotation profiles with different slopes and amplitudes for early-type dwarf galaxies in the Virgo cluster. The distribution of our galaxies in the $(v/\sigma)_e$ and λ_e versus ellipticity diagrams (Fig. 9) is not very different from that of the Virgo dwarfs as a whole population. Toloba et al. found 11 slow versus 28 fast rotators, while our sample has around half of the galaxies in either class (Fig. 9). Toloba et al. (2014b) concluded that ~ 6 per cent of early-type dwarfs have KDCs (see also Penny et al. 2016). One KDC in our sample of nine galaxies would be consistent with this frequency given the small number statistics.

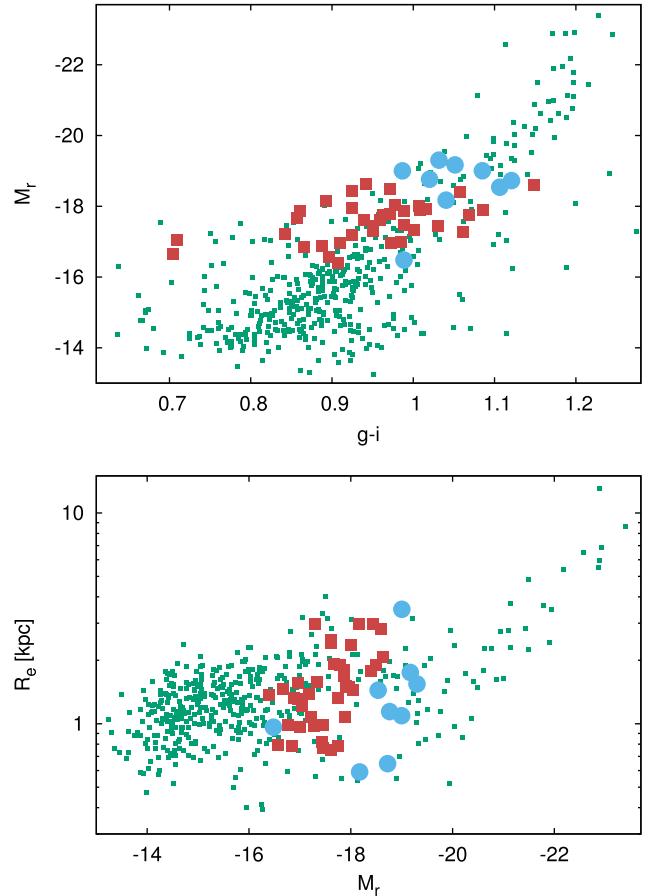


Figure 8. Colour–magnitude and size–magnitude relations. Shown are the Virgo early types (green dots; from Janz & Lisker 2008, 2009), the sample of Toloba et al. (2014a, red squares) and our galaxies (blue points – extinction-corrected 7 arcsec aperture colours). This comparison shows that the isolated quenched galaxies fall on the red sequence of the Virgo early types and span a very similar range of sizes.

6 DISCUSSION

6.1 Environmental dependences and isolation

One line of argument in favour of the ‘galaxy harassment in clusters’ scenario is the identification of a trend in some characteristic as a function of a quantification of the environment. For example, Toloba et al. (2015) found an increase of the spin parameter in the dwarfs in the Virgo cluster as a function of the (projected) distance to the cluster centre (cf. Fig. 9; see, however, Ryš, Falcón-Barroso & van de Ven 2013, who found with a smaller sample that such a trend is not significant when using 3D distances instead of projected ones), in this case given by the location of M87. Such a correlation of the spin parameter with clustercentric distance would be consistent with the finding that early-type dwarfs with signs of discs in their morphologies (Lisker et al. 2006a) are less clustered towards the centre than those without. Our isolated objects do not follow an extrapolation of such a trend, but instead show a similar variety of kinematic configurations as those in the Virgo cluster. We note that the analysis of dwarfs in galaxy groups by Penny et al. (2015) did not find any evidence in the kinematic scaling relations that would suggest a continuous change from the cluster centre to its outskirts to less rich groups and the field. We also note that higher

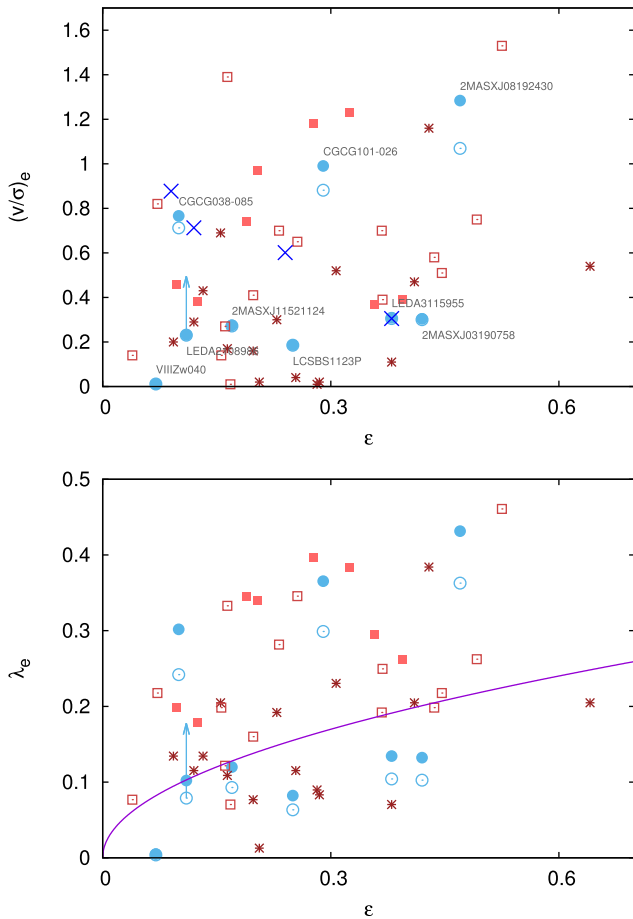


Figure 9. Upper panel: rotation parameter $(v/\sigma)_e$ as a function of ellipticity. Light blue open and filled symbols display the calculations for our sample galaxies assuming a surface brightness profile with Sérsic index $n = 1$ and 4, respectively. The arrow shows the shift for LEDA 2108986, when considering the alternative fit (see the text). The different red symbols show their Virgo early-type dwarfs [the boxes, circles and dots indicating small ($D < 2^\circ = 0.4 R_{\text{vir}}$; Ferrarese et al. 2012), intermediate and large projected distances ($D > R_{\text{vir}}$) to the cluster centre, respectively]. The blue crosses indicate the stellar kinematics of BCDs from Koleva et al. (2014). Lower panel: λ_e versus ellipticity with the same symbols. The purple line marks the demarcation line between slow and fast rotators from Toloba et al. (2015). There is no clear-cut difference in the kinematics of isolated early-type low-mass galaxies when compared to those in the Virgo cluster, and the four BCDs of Koleva et al. (2014) share the same parameter space.

mass early-type fast rotators do not show a correlation between local environment and spin parameter, although the slow rotators are more abundant in the highest densities of cluster cores. For the photometric scaling relations of early-type systems, de Rijcke et al. (2009) concluded that they are largely independent of the environment over a large range of mass.

A related, but separate topic is the (stellar population) age and colour of the galaxies, indicative of the time since the galaxy was quenched. Early-type dwarfs with blue centres in the Virgo cluster, i.e. with recent or residual star formation, do not show a clustering towards the cluster centre like other early-type dwarfs (Lisker et al. 2006b). The frequency of such objects increases with decreasing galaxy density of the environment: Pak et al. (2014) found blue centres in the early-type dwarfs of the Ursa Major cluster to be common. For the relatively unevolved NGC 5353/4 galaxy group,

Tully & Trentham (2008) asserted a large fraction of star-forming dwarfs with early-type morphology. Likewise, the prototype isolated early-type dwarf of Gu et al. (2006) has a blue core.

Our sample consists by construction (predominantly) of quenched objects. This means we will be missing a number of isolated galaxies that have early-type morphology but are still forming stars at some level. The fraction of early-type dwarfs with blue cores in the Virgo cluster that are excluded by our criteria for quenched galaxies (~ 52 per cent) gives a lower limit for this bias. In this context, the study of Peebles, Pogge & Stanek (2008) is of interest. Peebles et al. searched for outliers in the mass (gas-phase) metallicity relation. They identified 41 low-mass galaxies ($10^7 < M_* < 10^{10} M_\odot$) with overabundant oxygen. These galaxies form stars at some level, have early-type morphology and are typically fairly isolated without close companions. When the nearest-neighbour criteria of our search are employed, about half of their objects would be counted as isolated. Peebles et al. (2008) interpreted the high oxygen abundance with a low gas fraction and concluded that their galaxies are transitional dwarfs, evolving from star-forming to quenched early-type dwarfs.

The isolated quenched galaxies in our sample (median $M_* \sim 4 \times 10^9 M_\odot$ for the spectroscopic sample) suggest that galaxies at the high-mass end of the probed mass range can be quenched even without the cluster environment and its ram pressure stripping. This is consistent with the lower mass limit of Geha et al. (2012, $M_* < 10^9 M_\odot$) below which no isolated quenched galaxies were found. We note that our fiducial search criteria for isolated galaxies are less restrictive than the analysis of Geha et al. (2012). Their velocity interval for the neighbour search was 1000 km s^{-1} , while we use 500 km s^{-1} . Furthermore, Geha et al. (2012) found a definition of isolation in terms of the (projected) distance to the massive neighbour. The fraction of quenched galaxies as a function of the distance to the host flattens out at $\sim 1.5 \text{ Mpc}$. This applies for different mass bins and is consistent with our histogram in Fig. 2. The lowest mass object of those that we observed, LCBS1123P, has a neighbour at 1.2 Mpc with $M_{K_s} \sim -23 \text{ mag}$. We also note that 2MASX J08192430 has a luminous neighbour at $D_{\text{proj}} = 277 \text{ kpc}$ with a velocity difference of $\Delta V = 612 \text{ km s}^{-1}$. For the other eight objects, our classification does not change when increasing the velocity interval to 1000 km s^{-1} . This also applies to 28 of the 37 other candidates. When counting four times less massive galaxies as bright neighbours ($M_{K_s} = -21.5 \text{ mag}$; the completeness limit for our bright neighbour search; corresponding to $M_* \sim 8 \times 10^9 M_\odot$), the total numbers of candidates reduce to 17 and 12 for the 500 and 1000 km s^{-1} velocity difference intervals, respectively (see Table A1 in Appendix A). Even with the most stringent combination for the definition of isolation, i.e. a neighbour search extending to masses on the same order of magnitude as the low-mass galaxies within a velocity interval of $\pm 1000 \text{ km s}^{-1}$ and separations of at least 1.5 Mpc , five of the objects in our spectroscopic sample (and 11 of the complete sample of 46 galaxies) remain classified as isolated.

Summarizing this section: (i) our sample of quenched low-mass galaxies in the field does not follow a trend claimed in galaxy clusters of increasing spin parameter in dwarfs for decreasing local galaxy density; (ii) our sample consists by construction predominantly of quenched objects, while early-type dwarfs in low-density environments typically show signs of recent star formation; (iii) the classification as isolated objects is rather robust when it comes to the velocity interval that is considered for finding massive neighbours, but the numbers are approximately halved when considering also less massive neighbours; and (iv) while quenched dwarfs

are rare in the field, several examples at the high-mass end were identified.

6.2 Formation scenarios for isolated early-type dwarfs

In principle, isolated galaxies need not have lived in the field all their life (e.g. Chilingarian & Zolotukhin 2015). However, the distance to a more massive galaxy in our sample is $D_{\text{proj}} \gtrsim 1$ Mpc. This distance means a travel time of at least 1 Gyr with a relative velocity of 1000 km s^{-1} . Such a velocity exceeds the velocity dispersion of galaxies in the Virgo cluster (e.g. Binggeli, Popescu & Tammann 1993; $\sigma_{\text{Virgo}} \sim 700 \text{ km s}^{-1}$). Relative velocities more typical for less massive groups or galaxy pairs increase this hypothetical travel time to the order of a Hubble time.

If the isolated galaxies did not escape a high-density environment (or at least from a more massive host galaxy), the transformative processes associated with such environments, e.g. harassment and ram pressure stripping, cannot be the source for this galaxy population. In other words, these galaxies cannot be environmentally transformed spirals, and an alternative formation process needs to operate.

One possibility is dwarf–dwarf mergers, which were less frequently considered, since they are unlikely to happen where early-type dwarfs are predominantly found (i.e. in the cluster environment where large relative velocities make them difficult). However, recently observational evidence has mounted suggesting that such mergers (occasionally) happen (in other environments) and simulations have shown them to be a potential way to also form low-mass galaxies (van Zee, Skillman & Salzer 1998; Bekki 2008, 2015; Valcke, de Rijcke & Dejonghe 2008; Graham et al. 2012; Martinez-Delgado et al. 2012; Cloet-Osselaer et al. 2014; Pak et al. 2016; Watts & Bekki 2016). They were also suggested (in the context of pre-processing in galaxy groups) as a possible origin for KDCs in early-type dwarfs (Toloba et al. 2014b).

Another possibility is that the isolated quenched low-mass galaxies did not experience any dramatic events (such as mergers or harassment) in their past. Low-mass, pressure-supported, galaxies are expected to form as the first galaxies and constitute the building blocks in hierarchical structure formation and galaxy evolution. A disc can be grown and angular momentum can be obtained in a more steady fashion by gas accretion (and possibly minor mergers) from the cosmic web (see also Maccio, Moore & Stadel 2006), as also suggested for more massive early types (Dekel et al. 2009; Graham et al. 2015, and references therein). While this is not required or preferred, such gas accretion may even be feasible in the outskirts of the Virgo cluster as discussed by Hallenbeck et al. (2012).

In the context of gas accretion, LEDA 218986 is possibly the most intriguing object in our sample. It seems to be a candidate for the addition of gas, which is changing the internal kinematics, as well as being responsible for the emergence of KDCs (see also de Rijcke, Buyle & Koleva 2013) and for the creation of disc features in the image (see Graham et al. 2016 for details). These disc features resemble those in the Virgo cluster early-type dwarf galaxy VCC 216 (cf. Lisker, Brunngräber & Grebel 2009).

For the objects to be classified as quenched, the star formation activity needs to have ceased. One way is to cut off the gas supply, which is also consistent with the gas deficiency of the early-type dwarfs in clusters. For galaxies more massive than $M_* > 10^8 M_\odot$, supernova feedback is not sufficient to permanently expel the gas (Valcke et al. 2008). Observationally, Geha et al. (2012) did not find any quenched galaxies in the field with a stellar mass lower than

$M_* < 10^9 M_\odot$. While in clusters the gas supply can be removed by ram pressure stripping, this is not plausible for the most isolated objects. In principle, there could also be gas that just does not form stars. Or possibly, the gas may have been consumed some time ago for those galaxies in the field that are quenched today, leading to a ‘starvation’ similar to the scenario (with an external removal of the gas supply) proposed by Larson, Tinsley & Caldwell (1980, see also Boselli et al. 2008). The time-scale for the gas consumption might depend on galaxy mass (like the star formation time-scale, i.e. downsizing), and isolated galaxies with lower mass possibly did not have enough time to reach this stage. Regardless of the exact mechanisms involved, the dwarfs observed by Peebles et al. (2008, see above) appear to be good candidates for isolated galaxies with low gas fractions in their final stages before transitioning to being red and dead.

In this context, it is interesting to note that sometimes blue compact dwarf galaxies (BCDs) are considered as analogues of compact star-forming galaxies typical for earlier epochs of the Universe. It has been suggested that galaxies may evolve through several cycles of a BCD phase, characterized by intense star formation, and more quiescent phases, in which they resemble more normal low-mass late-type galaxies, to end up as early-type dwarfs after a final centrally concentrated star formation episode, after which the gas is consumed (Davies & Phillipps 1988). Also, some of the BCDs are observed to have low v/σ (Koleva et al. 2014), comparable to the early-type dwarfs (Fig. 9). The morphologies and circular rotation velocity gradient for both galaxy types were also found to compare favourable (Lelli, Fraternali & Verheijen 2014; Meyer et al. 2014). Moreover, the stellar populations of transition-type dwarfs appear to differ from those of early-type dwarfs only in the star formation activity at present day (Koleva et al. 2013, see also Peebles et al. 2008 and Michielsen et al. 2008 for a comparison of stellar population properties of early-type dwarfs in the Virgo cluster and less dense environments).

In summary, we consider both dwarf–dwarf mergers and gas accretion as viable candidates for explaining rotating quenched low-mass galaxies in isolation, bearing in mind also the earlier suggested evolutionary link between early-type dwarfs and BCDs.

6.3 Implications for early-type dwarfs in clusters

Our observation of rotating quenched low-mass galaxies in isolated environments indicates that the cluster environment need not have transformed spirals into early-type galaxies. This is because the field early-type galaxies have acquired their rotation from their formation as a less massive galaxy, rather than from the transformation of a more massive spiral galaxy.

The number of early-type dwarfs in the field versus groups versus clusters (e.g. Trentham & Tully 2002; Annibali et al. 2011) suggests that the high-density environment is still more prolific for forming early-type dwarfs. Before discussing this within the formation scenarios for isolated quenched low-mass galaxies, it should be noted that our observations do not rule out a contribution of processes related to the high-density environments (see Lisker 2009 for an overview, see also Morishita et al. 2017 for a perspective from higher redshift), such as harassment and ram pressure stripping to the population of early-type dwarfs in clusters. The latter may be required to quench the galaxies at lower stellar masses.

The formation scenarios discussed above can yield more galaxies in high-density environments than in the field for the following

reasons. First, a greater number of galaxies are expected to form in higher overdensities in the early Universe. Secondly, the high-density environment is likely to speed up the quenching by shutting off the gas supply, i.e. via ram pressure stripping (see also Grossi et al. 2009; Annibali et al. 2011; De Looze et al. 2013), and it can also quench galaxies below the mass limit of Geha et al. (2012), where there are no quenched galaxies in isolation. The galaxies in our sample are (mostly) more massive than those early-type dwarfs in the comparison sample for the Virgo cluster (the highest stellar mass in that sample is $M_* \sim 1.5 \times 10^9 M_\odot$). However, all of the galaxies in our sample can be considered as dwarfs when using the classical $M_B > -18$ mag criterion. We also note that the BCDs of Koleva et al. (2014, dynamical masses below $10^9 M_\odot$) and the objects in Peebles et al. (2008, 15 of them have $M_* < 10^9 M_\odot$) fit well into the mass range of the Virgo early-type dwarfs and are in this sense compatible with turning into early-type dwarfs after quenching.

The formation scenarios suggested for the quenched low-mass galaxies in isolation are also very attractive as a contributor to the early-type dwarf population in high-density environments. If the progenitor galaxy is a (more massive) spiral galaxy, the transformation has to alter its morphology, reduce the size and mass, and remove considerable amounts of angular momentum (Falcón-Barroso, Lyubenova & van de Ven 2015). This may even apply for some of the relatively low mass late-type galaxies at the end of the Hubble sequence (Adams et al. 2014; Janz et al. 2016). The only feasible way for a substantial transformation seems to be rather strong harassment. However, Smith et al. (2015) showed that this is unlikely to happen for galaxies falling into a cluster (cf. also Lisker, Weinmann, Janz & Meyer 2013; Bialas et al. 2015). The authors put rather conservative limits to the type of orbits that plausibly can lead to strong harassment and concluded that they are basically only likely for objects that were part of the cluster early on.

If the galaxy, instead of having a spiral galaxy as progenitor, has similar mass, size and little angular momentum to start with, strong harassment is not required. In some cases, angular momentum can be obtained by gas accretion and a disc might be grown. In other cases, the galaxies could remain pressure supported or grow by dwarf–dwarf mergers. Low-mass galaxies in the early Universe, with similar properties to some of the BCDs today (Koleva et al. 2014; Meyer et al. 2014; Lian et al. 2015; for simulations of dwarf–dwarf mergers forming BCDs and their rotation curves see also Watts & Bekki 2016), appear to be good candidates for evolving into galaxies similar to today’s early-type dwarf galaxies in the galaxy clusters. Since there is a mass limit observed below which quenched galaxies are absent in isolation ($M_* < 10^9 M_\odot$; Geha et al. 2012, i.e. in a mass range for which feedback is inefficient), gas removal via processes like ram pressure stripping appears to be required to quench galaxies below that mass limit today.

There is a long-lasting debate whether or not there is a structural dichotomy between dwarf and ordinary early-type galaxies, i.e. whether these galaxies follow distinct scaling relations brighter or fainter than $M_B = -18$ mag (e.g. Kormendy et al. 2009; Kormendy & Bender 2012; Graham 2013, and many references therein, see also Faber 1973 and Wirth & Gallagher 1984). For example, Graham & Guzmán (2003) showed that ordinary and dwarf early-type galaxies follow a log-linear relation of profile shape parametrized by the Sérsic index n (see also Jerjen & Binggeli 1997) with magnitude and demonstrated that this together with a continuous linear relation of central surface brightness and magnitude leads to curved, but continuous relations involving ‘effective’ or half-light

quantities, e.g. in the size–magnitude plane. With rebuttal of the necessity for a different formation scenario (i.e. galaxy harassment) for dwarf and ordinary early types, this question can be revisited. There are no signs for such a dichotomy in the spin parameter (i.e. when comparing Emsellem et al. 2011 and Toloba et al. 2015). The early-type dwarfs overlap in the spin parameter versus ellipticity diagram with the ordinary early types, but their parameter range is largely separate from that of the spiral galaxies. Furthermore, at intermediate mass, between the dwarf systems and the most massive galaxies, slow rotators are not frequent. The frequencies of KDCs in dwarf and ordinary early types are also comparable (Toloba et al. 2014b).

We conclude that the discovery of rotation in quenched low-mass galaxies in isolation shows that early-type dwarfs in clusters need not be harassed spirals. Furthermore, early-type dwarfs that are formed as low-mass galaxies, possibly quenched with the help of the clusters’ ram pressure, are an appealing contribution to the population of cluster dwarfs.

7 SUMMARY

We carried out a search for quenched low-mass galaxies in low galaxy density environments and isolation in the Local Volume of the SDSS. The criteria were a stellar mass below $M_* < 5 \times 10^9 M_\odot$, a strong 4000 Å break $D_n(4000) > 0.6 + 0.1 \times \log_{10}(M_*/M_\odot)$ and an H α equivalent width $EW_{H\alpha} < 2$ Å, and no massive neighbour ($M_* \gtrsim 3 \times 10^{10} M_\odot$) within a velocity interval of 500 km s^{-1} with a distance (in projection) $D_{\text{proj}} < 1$ Mpc. Our selection criteria yielded 46 galaxies. These were manually checked, e.g. for star formation missed by the SDSS fibre, and suitable candidates for spectroscopic follow-up were chosen. We observed nine of these objects with Keck ESI and have presented their internal kinematics based on the obtained spectra.

The nine objects exhibit a large variety of dynamic configurations: some show rotation velocities within R_e that exceed the random motions, while others have close to no rotation at all. In one case, we found signs of a kinematically decoupled inner region, which moves aligned with the counter-rotating ionized gas.

We compared our sample of isolated quenched low-mass galaxies to a sample of early-type dwarfs in the Virgo cluster. Both samples show similar characteristics: the galaxies have $M_B \gtrsim -18$ mag, they mostly lie on the red sequence and span a similar range of sizes. Likewise, their internal kinematics show a similar variety of behaviour, and the fractions of slow and fast rotations are compatible given the small number statistics.

The *rotating* quenched galaxies in our sample cannot be environmentally transformed spiral galaxies due to their isolation. This has an important implication: *early-type dwarfs in galaxy clusters need not be transformed spiral galaxies*.

We discussed dwarf–dwarf mergers and gas accretion as formation scenarios for our sample of isolated galaxies. Both of them should be able to produce the required range of angular momentum and degree of rotational support. Furthermore, we argued that these processes may contribute a greater number of early-type dwarfs to high-density environments than the small numbers of them found in the field. And ram pressure stripping can help to account for the quenched galaxies at lower stellar mass. Finally, we reasoned that given other challenges to the transformed spiral scenario such a contribution to the early-type dwarf population in galaxy clusters is appealing. The suggested formation scenarios are not exclusive, but their contribution can also help to explain the heterogeneity of early-type dwarf galaxies.

ACKNOWLEDGEMENTS

We thank the referee for suggestions that helped improve the presentation of our results. JJ and DAF thank the ARC for financial support via DP130100388. JJ also thanks T. Lisker for providing the non-parametric photometry code. SJP acknowledges financial support from the University of Portsmouth.

The NASA-Sloan Atlas was created by Michael Blanton, with extensive help and testing from Eyal Kazin, Guangtun Zhu, Adrian Price-Whelan, John Moustakas, Dimitri Muna, Renbin Yan and Benjamin Weaver.

Funding for SDSS-III has been provided by the Alfred P. Sloan Foundation, the Participating Institutions, the National Science Foundation and the US Department of Energy Office of Science. The SDSS-III website is <http://www.sdss3.org/>.

SDSS-III is managed by the Astrophysical Research Consortium for the Participating Institutions of the SDSS-III Collaboration including the University of Arizona, the Brazilian Participation Group, Brookhaven National Laboratory, Carnegie Mellon University, University of Florida, the French Participation Group, the German Participation Group, Harvard University, the Instituto de Astrofísica de Canarias, the Michigan State/Notre Dame/JINA Participation Group, Johns Hopkins University, Lawrence Berkeley National Laboratory, Max Planck Institute for Astrophysics, Max Planck Institute for Extraterrestrial Physics, New Mexico State University, New York University, Ohio State University, Pennsylvania State University, University of Portsmouth, Princeton University, the Spanish Participation Group, University of Tokyo, University of Utah, Vanderbilt University, University of Virginia, University of Washington and Yale University.

We acknowledge the usage of the HyperLeda data base (Makarov et al. 2014, <http://leda.univ-lyon1.fr>). This research has made use of the NASA/IPAC Extragalactic Database (NED), which is operated by the Jet Propulsion Laboratory, California Institute of Technology, under contract with the National Aeronautics and Space Administration. This research has made use of the SIMBAD data base, operated at CDS, Strasbourg, France.

This publication makes use of data products from the Two Micron All-Sky Survey, which is a joint project of the University of Massachusetts and the Infrared Processing and Analysis Center/California Institute of Technology, funded by the National Aeronautics and Space Administration and the National Science Foundation.

REFERENCES

Adams J. J. et al., 2014, *ApJ*, 789, 63
 Aguerri J. A. L., 2016, *A&A*, 587, A111
 Aguerri J. A. L., Iglesias-Páramo J., Vilchez J. M., Muñoz-Tuñón C., Sánchez-Janssen R., 2005, *AJ*, 130, 475
 Alam S. et al., 2015, *ApJS*, 219, 12
 Annibali F., Grützbauch R., Rampazzo R., Bressan A., Zeilinger W. W., 2011, *A&A*, 528, A19
 Argudo-Fernández M. et al., 2015, *A&A*, 578, A110
 Arnold J. A. et al., 2014, *ApJ*, 791, 80
 Barazza F. D., Binggeli B., Jerjen H., 2002, *A&A*, 391, 823
 Bekki K., 2008, *MNRAS*, 388, L10
 Bekki K., 2015, *ApJ*, 812, L14
 Berlind A. A. et al., 2006, *ApJS*, 167, 1
 Bernstein G. M., Jarvis M., 2002, *AJ*, 123, 583
 Bertin E., 2011, in Evans I. N., Accomazzi A., Mink D. J., Rots A. H., eds, *ASP Conf. Ser. Vol. 442, Astronomical Data Analysis Software and Systems XX*. Astron. Soc. Pac., San Francisco, p. 435
 Bertin E., Arnouts S., 1996, *A&AS*, 117, 393
 Bettoni D., 1989, *AJ*, 97, 79

Bialas D., Lisker T., Olczak C., Spurzem R., Kotulla R., 2015, *A&A*, 576, A103
 Binggeli B., Cameron L. M., 1991, *A&A*, 252, 27
 Binggeli B., Sandage A., Tammann G. A., 1988, *ARA&A*, 26, 509
 Binggeli B., Popescu C. C., Tammann G. A., 1993, *A&AS*, 98, 275
 Boselli A., Boissier S., Cortese L., Gavazzi G., 2008, *ApJ*, 674, 742
 Cappellari M., Emsellem E., 2004, *PASP*, 116, 138
 Carter D., Sadler E. M., 1990, *MNRAS*, 245, 12P
 Catinella B., Giovanelli R., Haynes M. P., 2006, *ApJ*, 640, 751
 Chilingarian I. V., 2009, *MNRAS*, 394, 1229
 Chilingarian I., Zolotukhin I., 2015, *Science*, 348, 418
 Cloet-Osselaer A., de Rijcke S., Vandenbroucke B., Schroyen J., Koleva M., Verbeke R., 2014, *MNRAS*, 442, 2909
 Davies J. I., Philipps S., 1988, *MNRAS*, 233, 553
 De Looze I. et al., 2013, *MNRAS*, 436, 1057
 de Rijcke S., Dejonghe H., Zeilinger W. W., Hau G. K. T., 2003, *A&A*, 400, 119
 de Rijcke S., Michielsen D., Dejonghe H., Zeilinger W. W., Hau G. K. T., 2005, *A&A*, 438, 491
 de Rijcke S., Penny S. J., Conselice C. J., Valcke S., Held E. V., 2009, *MNRAS*, 393, 798
 de Rijcke S., Buyle P., Koleva M., 2013, *ApJ*, 770, L26
 Dekel A. et al., 2009, *Nature*, 457, 451
 Eisenstein D. J. et al., 2011, *AJ*, 142, 72
 Emsellem E. et al., 2007, *MNRAS*, 379, 401
 Emsellem E. et al., 2011, *MNRAS*, 414, 888
 Faber S. M., 1973, *ApJ*, 179, 423
 Falcón-Barroso J., Lyubenova M., van de Ven G., 2015, in Cappellari M., Courteau S., eds, *Proc. IAU Symp. 311, Galaxy Masses as Constraints of Formation Models*. Cambridge Univ. Press, Cambridge, p. 78
 Ferguson H. C., Binggeli B., 1994, *A&AR*, 6, 67
 Ferrarese L. et al., 2012, *ApJS*, 200, 4
 Forbes D. A., Spitler L. R., Graham A. W., Foster C., Hau G. K. T., Benson A., 2011, *MNRAS*, 413, 2665
 Foster C. et al., 2016, *MNRAS*, 457, 147
 Freeman K. C., 1970, *ApJ*, 160, 811
 Fuse C., Marcum P., Fanelli M., 2012, *AJ*, 144, 57
 Geha M., Guhathakurta P., van der Marel R. P., 2002, *AJ*, 124, 3073
 Geha M., Guhathakurta P., van der Marel R. P., 2003, *AJ*, 126, 1794
 Geha M., Blanton M. R., Yan R., Tinker J. L., 2012, *ApJ*, 757, 85
 Giovanelli R., Haynes M. P., 2002, *ApJ*, 571, L107
 Graham A. W., 2013, *Planets, Stars and Stellar Systems*. Springer, Berlin p. 91
 Graham A., Colless M., 1997, *MNRAS*, 287, 221
 Graham A. W., Guzmán R., 2003, *AJ*, 125, 2936
 Graham A. W., Driver S. P., Petrosian V., Conselice C. J., Bershadsky M. A., Crawford S. M., Goto T., 2005, *AJ*, 130, 1535
 Graham A. W., Spitler L. R., Forbes D. A., Lisker T., Moore B., Janz J., 2012, *ApJ*, 750, 121
 Graham A. W., Dullo B. T., Savorgnan G. A. D., 2015, *ApJ*, 804, 32
 Graham A. W., Janz J., Penny S. J., Chilingarian I., Ciambur B. C., Forbes D. A., Davies R. L., 2017, *ApJ*, in press
 Grossi M. et al., 2009, *A&A*, 498, 407
 Gu Q., Zhao Y., Shi L., Peng Z., Luo X., 2006, *AJ*, 131, 806
 Gunn J. E., Gott J. R. I., 1972, *ApJ*, 176, 1
 Hallenbeck G. et al., 2012, *AJ*, 144, 87
 Huchra J. P. et al., 2012, *ApJS*, 199, 26
 Janz J., Lisker T., 2008, *ApJ*, 689, L25
 Janz J., Lisker T., 2009, *ApJ*, 696, L102
 Janz J. et al., 2012, *ApJ*, 745, L24
 Janz J. et al., 2014, *ApJ*, 786, 105
 Janz J., Laurikainen E., Laine J., Salo H., Lisker T., 2016, *MNRAS*, 461, L82
 Jerjen H., Binggeli B., 1997, in Arnaboldi M., Da Costa G. S., Saha P., eds, *ASP Conf. Ser. Vol. 116, The Nature of Elliptical Galaxies*. Astron. Soc. Pac., San Francisco, p. 239
 Jerjen H., Kalnajs A., Binggeli B., 2000, *A&A*, 358, 845

Koleva M., Bouchard A., Prugniel P., de Rijcke S., Vauglin I., 2013, *MNRAS*, 428, 2949

Koleva M., de Rijcke S., Zeilinger W. W., Verbeke R., Schroyen J., Vermeulen L., 2014, *MNRAS*, 441, 452

Kormendy J., Bender R., 2012, *ApJS*, 198, 2

Kormendy J., Fisher D. B., Cornell M. E., Bender R., 2009, *ApJS*, 182, 216

Larson R. B., Tinsley B. M., Caldwell C. N., 1980, *ApJ*, 237, 692

Lelli F., Fraternali F., Verheijen M., 2014, *A&A*, 563, A27

Lian J. H., Kong X., Jiang N., Yan W., Gao Y. L., 2015, *MNRAS*, 451, 1130

Lisker T., 2009, *Astron. Nachr.*, 330, 1043

Lisker T., Grebel E. K., Binggeli B., 2006a, *AJ*, 132, 497

Lisker T., Glatt K., Westera P., Grebel E. K., 2006b, *AJ*, 132, 2432

Lisker T., Brunngräber R., Grebel E. K., 2009, *Astron. Nachr.*, 330, 966

Lisker T., Weinmann S. M., Janz J., Meyer H. T., 2013, *MNRAS*, 432, 1162

Maccio A. V., Moore B., Stadel J., 2006, *ApJ*, 636, L25

Makarov D., Prugniel P., Terekhova N., Courtois H., Vauglin I., 2014, *A&A*, 570, A13

Martinez-Delgado D. et al., 2012, *ApJ*, 748, L24

Mayer L., Governato F., Colpi M., Moore B., Quinn T., Wadsley J., Stadel J., Lake G., 2001, *ApJ*, 547, L123

Meyer H. T., Lisker T., Janz J., Papaderos P., 2014, *A&A*, 562, A49

Michielsen D. et al., 2008, *MNRAS*, 385, 1374

Moore B., Katz N., Lake G., Dressler A., Oemler A., 1996, *Nature*, 379, 613

Morishita T. et al., 2017, *ApJ*, 835, 254

Naab T. et al., 2014, *MNRAS*, 444, 3357

Pak M., Rey S.-C., Lisker T., Lee Y., Kim S., Sung E.-C., Jerjen H., Chung J., 2014, *MNRAS*, 445, 630

Pak M., Paudel S., Lee Y., Kim S. C., 2016, *AJ*, 151, 141

Pedraz S., Gorgas J., Cardiel N., Sánchez-Blázquez P., Guzmán R., 2002, *ApJ*, 332, L59

Peeples M. S., Pogge R. W., Stanek K. Z., 2008, *ApJ*, 685, 904

Peng C. Y., Ho L. C., Impey C. D., Rix H.-W., 2010, *AJ*, 139, 2097

Penny S. J., Forbes D. A., Pimblet K. A., Floyd D. J. E., 2014, *MNRAS*, 443, 3381

Penny S. J., Janz J., Forbes D. A., Benson A. J., Mould J., 2015, *MNRAS*, 453, 3635

Penny S. J. et al., 2016, *MNRAS*, 462, 3955

Ryś A., Falcón-Barroso J., van de Ven G., 2013, *MNRAS*, 428, 2980

Ryś A., van de Ven G., Falcón-Barroso J., 2014, *MNRAS*, 439, 284

Sánchez-Janssen R., Méndez-Abreu J., Aguerri J. A. L., 2010, *MNRAS*, 406, L65

Schlegel D. J., Finkbeiner D. P., Davis M., 1998, *ApJ*, 500, 525

Scott N., Davies R. L., Houghton R. C. W., Cappellari M., Graham A. W., Pimblet K. A., 2014, *MNRAS*, 441, 274

Sheinis A. I., Bolte M., Epps H. W., Kibrick R. I., Miller J. S., Radovan M. V., Bigelow B. C., Sutin B. M., 2002, *PASP*, 114, 851

Smith R. et al., 2015, *MNRAS*, 454, 2502

Sparke L. S., Sellwood J. A., 1987, *MNRAS*, 225, 653

Tadaki K.-i. et al., 2017, *ApJ*, 834, 135

Terzić B., Graham A. W., 2005, *MNRAS*, 362, 197

Toloba E. et al., 2014a, *ApJS*, 215, 17

Toloba E. et al., 2014b, *ApJ*, 783, 120

Toloba E. et al., 2015, *ApJ*, 799, 172

Trentham N., Tully R. B., 2002, *MNRAS*, 335, 712

Tully R. B., Trentham N., 2008, *AJ*, 135, 1488

Valcke S., de Rijcke S., Dejonghe H., 2008, *MNRAS*, 389, 1111

van Zee L., Skillman E. D., Salzer J. J., 1998, *AJ*, 116, 1186

Watts A., Bekki K., 2016, *MNRAS*, 462, 3314

Wirth A., Gallagher J. S. I., 1984, *ApJ*, 282, 85

APPENDIX A: ALTERNATIVE NEIGHBOUR SEARCH

Here we include the parameters of the nearest bright neighbour when searching for neighbours with $M_{K_s} < -21.5$ mag (Table A1).

Table A1. Projected distances and velocity differences for luminous neighbours with $M_{K_s} < -21.5$ mag.

Galaxy	Closest luminous neighbour			
	D_{500} (Mpc)	$ \Delta V_{500} $ (km s ⁻¹)	D_{1000} (Mpc)	$ \Delta V_{1000} $ (km s ⁻¹)
LEDA 3115955	1.67	13		
2MASX J03190758+4232179	0.63	311	0.55	586
LCSBS1123P	1.24	167		
2MASX J08192430+2100125	0.20	203	0.06	950
VIII Zw 040	3.47	62		
CGCG038-085	2.03	75		
2MASX J11521124+0421239	3.14	166	1.38	662
CGCG101-026	2.40	263		
LEDA 2108986	3.07	21		
J001212.41-110010.4	0.10	29		
J001530.03+160429.7	0.21	384		
J001601.19+160133.4	0.34	214		
J012506.69-000807.0	0.67	293		
J013842.89-002053.0	0.53	80		
J045058.77+261313.7	1.90	305	1.83	661
J075303.96+524435.8	1.04	63		
J082013.92+302503.0	0.88	97		
J082210.66+210507.5	0.16	482		
J084915.01+191127.3	0.22	500	0.11	526
J085652.63+475923.8	3.67	277		
J091514.45+581200.3	1.53	58		
J091657.98+064254.2	0.77	66		
J093016.38+233727.9	0.04	52		
J093251.11+314145.0	1.72	209		
J094408.52+111514.8	0.08	84		
J094834.50+145356.6	0.46	94		
J100003.93+044845.0	0.19	66		
J105005.53+655015.6	0.10	162		
J110423.34+195501.5	0.56	263		
J112422.89+385833.3	1.30	354	0.06	925
J114423.13+163304.5	1.21	331	0.02	549
J120300.94+025011.0	1.06	55		
J120823.99+435212.4	0.77	27		
J122543.23+042505.4	0.11	209		
J124408.62+252458.2	0.14	2		
J125026.61+264407.1	0.04	200		
J125103.34+262644.6	0.44	373		
J125321.68+262141.1	0.22	360		
J125756.52+272256.2	0.26	369		
J125940.10+275117.7	4.20	123	0.04	936
J130320.35+175909.7	1.04	164	0.96	553
J130549.09+262551.6	0.91	207		
J142914.46+444156.3	0.89	82		
J144621.10+342214.1	1.97	379		
J160810.70+313055.0	5.52	72		
J232028.21+150420.8	1.02	438	0.84	559

Notes. The first column lists the galaxy name. The closest bright neighbour within a velocity interval of ± 500 km s⁻¹ is extracted from a combined catalogue containing redshifts from the NASA-Sloan Atlas and the 2MASS redshift survey. Instead of $M_{K_s} < -23$ mag as in Table 1, $M_{K_s} < -21.5$ mag is used. The projected (linear) distance between the neighbour and the low-mass galaxy and the difference between their recession velocities are given in columns 2 and 3. If there is an additional neighbour within a velocity interval of ± 1000 km s⁻¹, the corresponding details are listed in columns 4 and 5.

This paper has been typeset from a \LaTeX file prepared by the author.